

Structural, Magnetic, and Dielectric Properties of $\text{Ni}_{0.5}\text{Zn}_{0.5}\text{Al}_x\text{Fe}_{2-x}\text{O}_4$ Nanoferrites

B. Rajesh Babu¹ · K. V. Ramesh² · M. S. R. Prasad³ · Y. Purushotham⁴

Received: 8 October 2015 / Accepted: 16 December 2015 / Published online: 15 January 2016
© Springer Science+Business Media New York 2016

Abstract This work investigates the effect of non-magnetic aluminum (Al) substitution in structural, morphological, magnetic, and dielectric properties of nanosized $\text{Ni}_{0.5}\text{Zn}_{0.5}\text{Al}_x\text{Fe}_{2-x}\text{O}_4$ ($0.0 \leq x \leq 0.25$) synthesized through citrate-gel autocombustion route (CGAC). Structural characterizations were performed by using X-ray powder diffraction (XRD), FT-IR, and scanning electron microscope (SEM). XRD reveals the formation of single-phase cubic spinel with crystallite sizes around 62–57 nm for all Al substituted samples estimated from Williamson-Hall method. Two significant absorption bands around 600 cm^{-1} and 400 cm^{-1} are observed from FT-IR spectra of samples under investigation, which confirms the formation of a single-phase cubic spinel. Interionic bond lengths and bond angles confirm the solubility of Al in the spinel lattice and support the observed variation in magnetic properties. Using vibrating sample magnetometer (VSM) saturation magnetization, coercivity has been measured. A decrease in lattice

parameter, saturation magnetization with increasing Al concentration was attributed to the difference in the ionic radii and weakening of exchange interactions. The decrease in initial permeability explained on the basis of variation in grain size and porosity. Dielectric constant and dielectric loss decreases with increasing Al concentration and with frequency.

Keywords Ni-Zn-Al ferrite · Citrate-gel autocombustion · Electron microscopy · Grain size · Permeability · Dielectric constant

1 Introduction

Spinel ferrites are important class of magnetic materials having wide variety of applications in electromagnetic devices due to their remarkable electrical, magnetic, and optical properties [1]. Over the years, researchers are intended to synthesize and study nanoferrites due to their excellent properties at nanorange [2]. This significant variation when the particle size reduced to nanoscale is majorly due to increased surface area and quantum effects. Among the spinel ferrites, Ni-Zn ferrites are excellent core materials for power transformers in electronic and telecommunication applications due to their low coercivity and high electrical resistivity. However, the performance of these ferrites are dictated by the preparation methods, sintering temperature, chemical composition, substitution of cations, and their distribution among the tetrahedral (A) and octahedral (B) sites. Researchers attempted to enhance the performance and versatility of these ferrites by incorporating minor amount of dopants in to the Ni-Zn ferrite

✉ K. V. Ramesh
kv_ramesh5@yahoo.co.in

¹ Department of Physics, G.V.P. College of Engineering for Women, Visakhapatnam, India

² Department of Physics, MVGR College of Engineering, Chintalavalasa, Vizianagaram, India

³ Department of Physics, GIS, GITAM University, Rushikonda, Visakhapatnam, India

⁴ Centre for Materials for Electronics Technology (C-MET), Cherlapally, Hyderabad, India

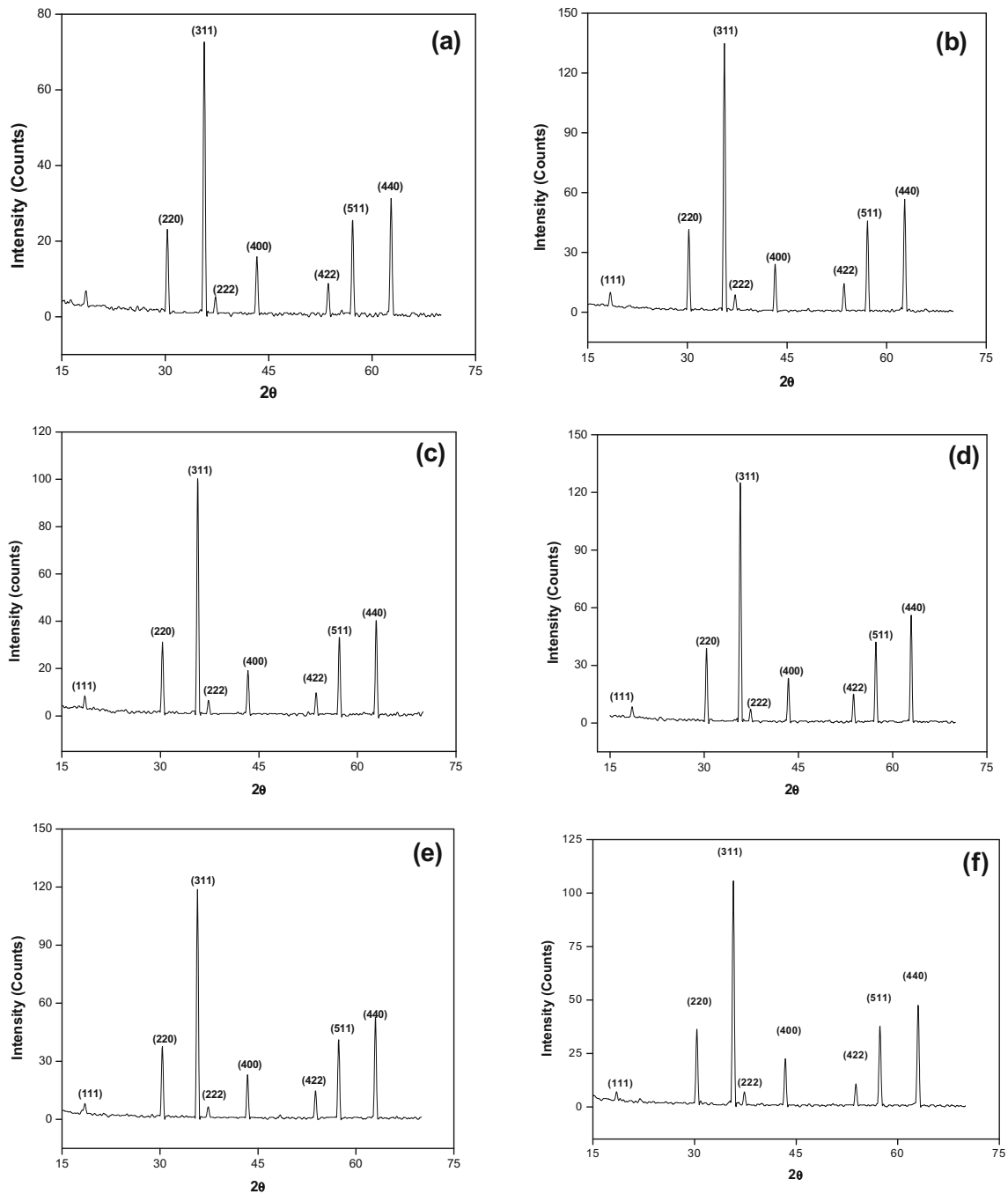


Fig. 1 X-ray diffraction patterns of $\text{Ni}_{0.5}\text{Zn}_{0.5}\text{Al}_x\text{Fe}_{2-x}\text{O}_4$. **a** $x = 0.0$. **b** $x = 0.05$. **c** $x = 0.1$. **d** $x = 0.15$. **e** $x = 0.2$. **f** $x = 0.25$

system [3–7]. Several authors reported that substitution of diamagnetic Al enhances the performance of the ferrites [8–12]. We have previously reported the influence of Al substitution at the expense of ferric ions in Ni–Zn nanoferrites [13–15]. In this article, the reports are mainly focused on synthesis and detailed investigation on changes takes place in structural, magnetic and dielectric properties due to the substitution of Al in $\text{Ni}_{0.5}\text{Zn}_{0.5}\text{Fe}_2\text{O}_4$ nanoferrite.

2 Experimental

Nanoparticles of $\text{Ni}_{0.5}\text{Zn}_{0.5}\text{Al}_x\text{Fe}_{2-x}\text{O}_4$ ($0.0 \leq x \leq 0.25$) have been prepared by citrate-gel autocombustion method which can be found in our recent work [14]. XRD measurements were carried out on powder samples using PANalytical X'Pert Pro diffractometer with $\text{Cu-K}\alpha$ radiation at room temperature to confirm the structure and phase purity of the prepared samples. The intensities were recorded for

Table 1 Lattice constant, crystallite size, and oxygen parameters of Ni_{0.5}Zn_{0.5}Al_xFe_{2-x}O₄ sintered at 1000 °C

Concentration (x)	a _o (Å)	Crystallite size (nm)	u ^{3m} (Å)	u ^{43m} (Å)	u ^{43m} (Å)	u ^{43m} (Å)
0	8.39	62	0.25749	0.38249	0.38244	0.38255
0.05	8.383	60	0.25747	0.38247	0.38247	0.38252
0.1	8.375	56	0.25745	0.38245	0.38241	0.38249
0.15	8.368	58	0.25743	0.38243	0.38241	0.38246
0.2	8.36	58	0.25734	0.38234	0.38237	0.38235
0.25	8.353	57	0.25739	0.38239	0.38239	0.3824

20°–80° with a step scan of 0.03°/s. The infrared spectra for all the samples were recorded with FT-IR spectrophotometer (Shimadzu FT-IR Prestige21) using KBr pellets in the range 4000–300 cm⁻¹. The surface morphology of the sintered ferrite powders was analyzed by using LEO 435 VP microscope (accelerating voltage up to 30 kV). Magnetic measurements have been carried out on LAKESHORE VSM 7410 magnetometer up to a maximum field of 1.5 Tesla. The inductance (L) was measured using HP4192A LF Impedance analyzer at the small voltage of 1 mV over a frequency of range 1 K to 13 MHz. The percentage of porosity of each sample was calculated using the relation $P(\%) = [1 - (d/d_x)] \times 100$, where d is bulk density and d_x is X-ray density. Permeability was computed using the relation $\mu = L/L_o$. Here $L_o = 4.606 \log(OD/ID) N^2 nH$ is the air core inductance; N is the number of turns; and OD and ID are outer and inner diameters of the toroid. Dielectric constant and loss have been measured using HP4192A LF Impedance analyzer.

3 Results and Discussion

3.1 Structural Properties

The X-ray diffraction (XRD) patterns of Ni_{0.5}Zn_{0.5}Al_xFe_{2-x}O₄ ($x = 0.00 - 0.25$ in steps of 0.05) powders sintered at 1000 °C is shown in Fig. 1. The formation of spinel ferrite phase was confirmed with JCPDS file no. 08-0234 from the intense X-ray diffraction lines corresponding to (220) (311) (222) (400) (422) (511) (440) planes using a standard diffraction plot [16]. The decrease in the lattice parameter (Table 1) with Al³⁺ ion substitution is ascribed to the ionic radius difference between the substituted Al³⁺ (0.051 nm) and the displaced Fe³⁺ (0.064 nm) ions which is in accordance with Vegard’s law [17]. The variation of lattice constant with Al³⁺ substitution inevitably supports the occupancy of the Al ions into the host Ni–Zn ferrite lattice.

The spinel unit cell is comprised of eight formulae units of AB₂O₄, belongs to the space group Fd $\bar{3}$ m. The tetrahedral (A) site is smaller than the octahedral (B) site. The local distortion among the sites (A and B) takes place while accommodating the available cations. Thus, each A site expands by an equal displacement of the four surrounding oxygen ions, towards and along the body diagonal of the cube, to form a tetrahedral with an “A” ion having cubic symmetry. However, six oxygen ions surrounding a “B” site are shifted in such a way that this oxygen octahedral shifts by the same amount, as the first expands. The difference in the expansion of octahedral site and tetrahedral sites is characterized by a parameter named as “oxygen parameter (u)”, which gives the distance between an oxygen ion and a face of a cube. Considerable changes could be expected to a significant extent due to the substitution of Al³⁺ ions in oxygen positional parameter (u), octahedral and tetrahedral bond lengths, bond-edges, cation–anion (M_e-O), cation–cation (M_e-M_e) distances and bond angles. In general, a clear understanding of the above parameters is essential because any adjustment in the structure due to incorporation of a dopant would alter the exchange interactions in the spinel lattice, which in turn influences the magnetic, electrical, and dielectric properties of the ferrites.

In order to calculate the oxygen parameter one has to choose the origin of the unit cell in the Fd $\bar{3}$ m space group. The origin of the unit cell in spinel is taken as either at 4 $\bar{3}$ m (with A site cation) or $\bar{3}$ m (with B site cation) [18]. The anion parameter (u) has been obtained from the expressions given as follows [19].

$$\text{Center of symmetry at } \left(\frac{1}{4} \frac{1}{4} \frac{1}{4}\right) \quad \text{Center of symmetry at } \left(\frac{3}{8} \frac{3}{8} \frac{3}{8}\right)$$

$$u^{3m} = \frac{R^2 - \frac{2}{3} + \sqrt{\frac{11}{48}R^2 - \frac{1}{18}}}{2R^2 - 2} \quad u^{43m} = \frac{R^2 - \frac{11}{12} + \sqrt{\frac{11}{48}R^2 - \frac{1}{18}}}{2R^2 - 2}$$

$$u^{43m} = \frac{r_A + R_O}{a\sqrt{3}} + \frac{1}{4}$$

$$u^{43m} = 0.3876 \left(\frac{r_B}{r_A}\right)^{-0.07054}$$

where R is the ratio of octahedral to tetrahedral bond lengths respectively (given $R = \frac{(B-O)}{(A-O)} = \frac{r_B + R_O}{r_A + R_O}$, r_A

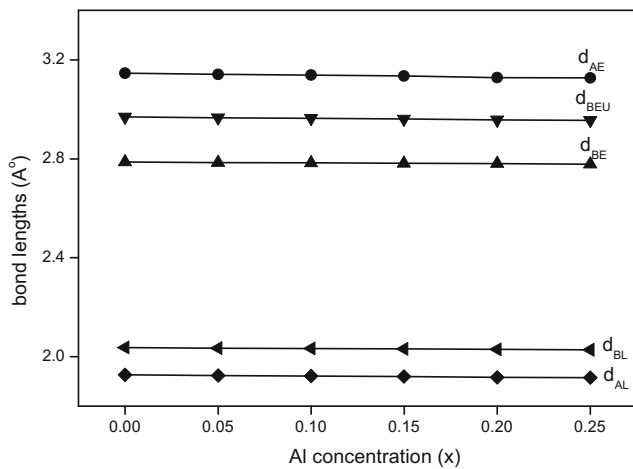


Fig. 2 Variations in bond lengths of $\text{Ni}_{0.5}\text{Zn}_{0.5}\text{Al}_x\text{Fe}_{2-x}\text{O}_4$

and r_B are the average ionic radius of the cations at A and B sites calculated based on the proposed cation distribution respectively and R_O is the radius of oxygen). In general, the oxygen parameter values for an ideal spinel u_{ideal}^{43m} is 0.375, while u_{ideal}^{3m} is 0.250. In order to convert the origin from A site to B site the following relation was used:

$$u^{43m} = u^{3m} + \frac{1}{8}$$

However, slight deviation from the perfect value may occur due to relatively larger oxygen ion which causes a small distortion of the lattice structure to make space for the cations at the available interstitial sites in the unit cell. Table 1 shows the oxygen positional parameters of Ni–Zn–Al ferrite sintered at 1000 °C. It is clear that the oxygen positional parameter (u^{43m}) calculated from various formulae are in good agreement with each other. Using the experimental lattice constant and oxygen

parameter shared and unshared tetrahedral, octahedral bond lengths are computed by using the following expressions:

Shared tetrahedral edge	$d_{AE} = a\sqrt{2}\left(2u^{43m} - \frac{1}{2}\right)$
Shared octahedral edge	$d_{BE} = a\sqrt{2}(1 - 2u^{43m})$
Unshared octahedral edge	$d_{BEU} = a\left[4(u^{43m})^2 - 3u^{43m} + \frac{11}{16}\right]^{1/2}$
Tetrahedral bond length	$d_{AL} = a\sqrt{3}\left(u^{43m} - \frac{1}{4}\right)$
Octahedral bond length	$d_{BL} = a\left[3(u^{43m})^2 - \frac{11}{4}u^{43m} + \frac{43}{64}\right]^{1/2}$

Figure 2 clearly shows that the bond lengths have been decrease with increasing Al concentration. The decrease in tetrahedral (d_{AL}) and octahedral (d_{BL}) bond lengths are due to the replacement of Fe^{3+} ions by Al^{3+} ions. The reduction in bond lengths would affects the exchange interactions (magnetic property) and hoping probability (electrical conductivity) between the cations in A and B sites. Figure 3 depicts the favorable distances and bond angles for ideal spinel ferrite between the metal ions. The interionic distances between cations (Me–Me) (b,c,d,e and f) and between the cation and anion (M_e-O) (p,q,r,s) were calculated using the experimental lattice constant (a_0) and oxygen parameter (u^{3m}) by using the following relations available in the literature [20, 21].

$M_e-M_e(\text{Å})$	$M_e-O(\text{Å})$
$b = (a_0/4)\sqrt{2}$	$p = a_0(1/2 - u^{3m})$
$c = (a_0/8)\sqrt{11}$	$q = a_0(u^{3m} - 1/8)\sqrt{3}$
$d = (a_0/4)\sqrt{3}$	$r = a_0(u^{3m} - 1/8)\sqrt{11}$
$e = (3a_0/8)\sqrt{3}$	$s = a_0/3(u^{3m} + 1/2)\sqrt{3}$
$f = (a_0/4)\sqrt{6}$	

The changes in the interionic bond lengths and bond angles between the cation–cation (M_e-M_e) and cation–anion (M_e-O) alters the overall strength of the magnetic interactions (A–A, B–B, and A–B) in A and B sublattices. The bond angles ($\theta_1, \theta_2, \theta_3, \theta_4$ and θ_5) have been evaluated by simple trigonometric equations and the calculated values are listed in Table 2. It is found that

Fig. 3 Interionic distances and bond angles for ideal spinel ferrite between the metal ions

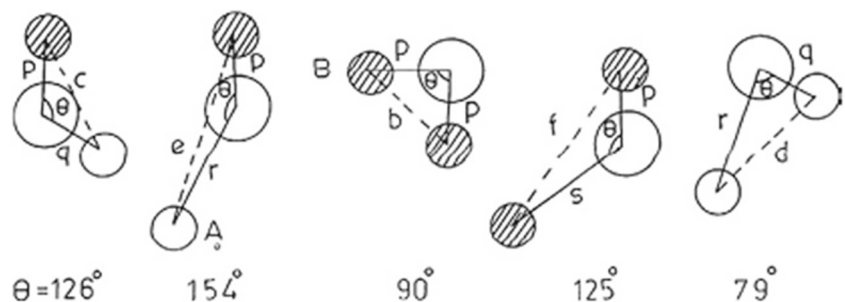


Table 2 Interionic distances and bond angles for Ni_{0.5}Zn_{0.5}Al_xFe_{2-x}O₄sintered at 1000 °C

Composition (x)	0.0	0.05	0.1	0.15	0.2	0.25
p (Å)	2.0352	2.0327	2.0317	2.0298	2.028	2.0261
q (Å)	1.9258	1.923	1.9216	1.9194	1.9156	1.915
r (Å)	3.6877	3.6823	3.6795	3.6753	3.6681	3.6669
s (Å)	3.6702	3.6653	3.663	3.6593	3.6542	3.6518
b (Å)	2.9671	2.9632	2.9614	2.9585	2.9547	2.9526
c (Å)	3.4792	3.4746	3.4726	3.4691	3.4647	3.4622
d (Å)	3.6339	3.6291	3.627	3.6234	3.6187	3.6161
e (Å)	5.4508	5.4437	5.4404	5.435	5.4281	5.4242
f (Å)	5.1391	5.1323	5.1293	5.1242	5.1176	5.114
θ ₁ ^o	122.93	122.94	122.95	122.95	122.98	122.97
θ ₂ ^o	142.97	143	143.03	143.05	143.17	143.11
θ ₃ ^o	93.65	93.64	93.63	93.62	93.57	93.6
θ ₄ ^o	126.15	126.15	126.15	126.14	126.13	126.14
θ ₅ ^o	73.25	73.27	73.29	73.3	73.38	73.34

(Table 2) both inter-ionic distances between the cation–anion and between cations decreases with increasing Al concentration (x). This result is in accordance with decrease in length of tetrahedral (d_{AE}) and octahedral (d_{BE}) edge. The observed decrease in interionic angles (θ₁θ₂ and θ₅) suggests the strengthening of A–B and A–A interactions. In spinel ferrites, the strong exchange interaction between A–B and B–B cations would tailor the magnetic properties.

3.1.1 Crystallite Size and Strain Analysis

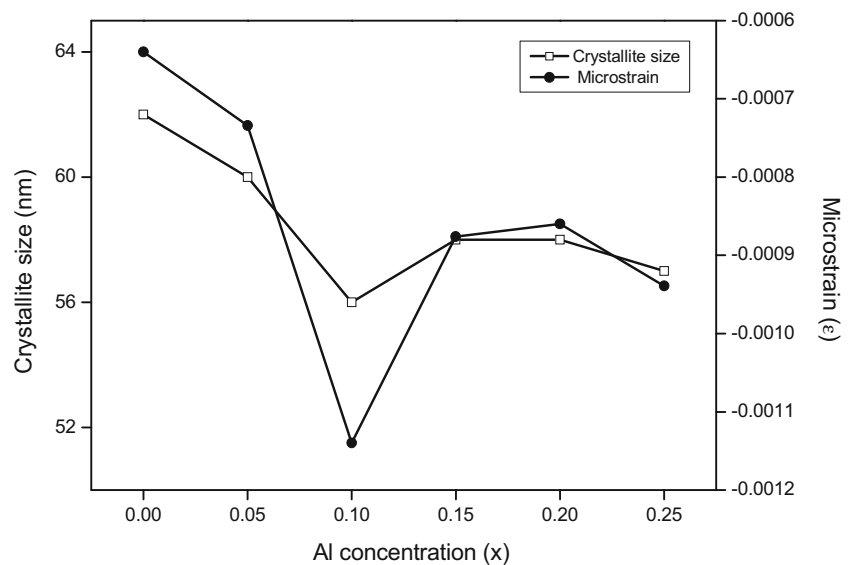
The average crystallite (t_{WH}) size estimated by using Williamson–Hall (W-H) method [22] is listed in Table 1.

W-H analysis is the simplified integral breadth method by which one can compute the crystallite size by separating size and strain broadenings as follows:

$$\frac{\beta \cos \theta}{\lambda} = \frac{1}{D} + \frac{4\varepsilon \sin \theta}{\lambda}$$

where β is experimentally observed FWHM size, ε is micro strain coefficient, D is the crystallite size, θ is incident angle of the X-rays and λ is the wave length of the target material used. From the linear fit to the data, the crystallite size was estimated from Y-intercept, and the strain ε, from the slope of the fit and is shown in Fig. 4.

Fig. 4 Variation of crystallite size and microstrain (ε) with Al concentration



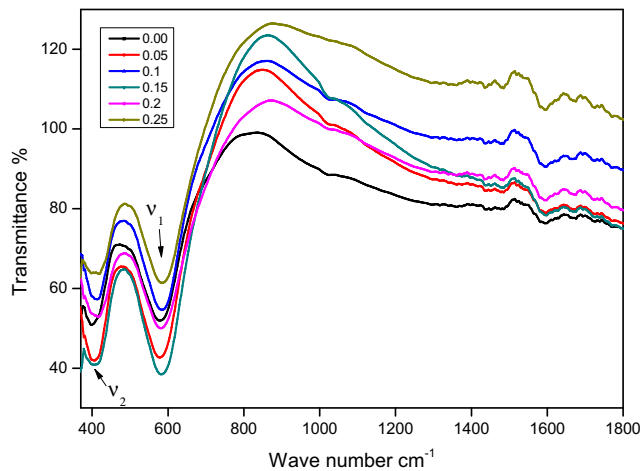


Fig. 5 FT-IR spectra of $\text{Ni}_{0.5}\text{Zn}_{0.5}\text{Al}_x\text{Fe}_{2-x}\text{O}_4$ system

3.2 Infrared Spectroscopic Analysis

The IR analysis also supports the formation of single phase Ni–Zn–Al ferrite. Figure 5 shows IR spectra of the Al substituted Ni–Zn nanoferrites in the frequency range of 400 to 1800 cm^{-1} . Two major absorption bands labeled as ν_1 and ν_2 which corresponds to the vibrations of the tetrahedral sites (A–O–A bonds) and the octahedral sites (B–O–B bonds), respectively [23]. The higher wave number band (ν_1) for all the samples shifts from 578.64 to 584.43 cm^{-1} and lower wave number (ν_2) shifts from 399.26 to 418.55 cm^{-1} with increasing Al concentration. The observed shift in the peaks is expected and is due to modification in the occupation of the cations in tetrahedral (A) and octahedral (B) sites. It is well known that, the change in bond length has an inverse relation with the band frequency shift [24]. Therefore, such increase in the frequency of absorption is due to the decrease in tetrahedral and octahedral bond lengths. The absorption peaks between

1000 and 1700 cm^{-1} are ascribed to the minor amount of unreacted citric acid [25].

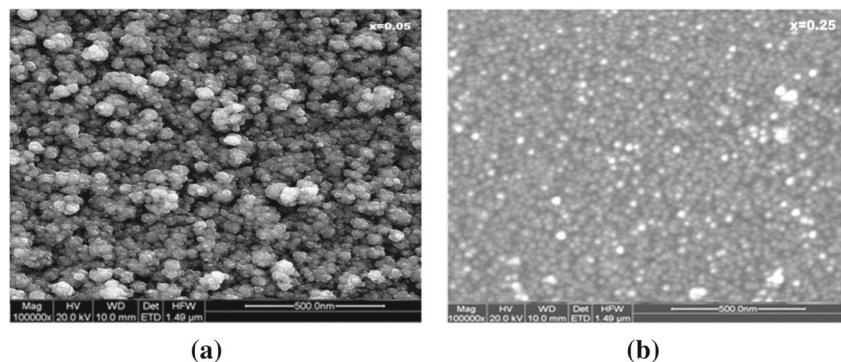
3.3 Microstructure

Microstructure plays an important role in dictating the electrical and magnetic properties of the spinel ferrite. SEM images of Ni–Zn–Al ferrites sintered at 1000 °C are shown in Fig. 6. It is evident that substitution of Al in Ni–Zn ferrite modifies the microstructure. The morphology for all the samples displayed nearly uniform, spherical, independent submicron grains with a soft agglomeration and with narrow grain size distribution. Grain size (D) has been computed using Image J 1.48 V software. It is clear that grain sizes of all the samples are found to be in the range 383–27 nm. Decrease in grain size with increasing Al concentration is consistent with the reported literature [26, 27]. The effects of grain size on magnetic permeability and dielectric properties are discussed in Sections 3.4 and 3.5.

3.4 Magnetic Properties

The significant properties of Ni–Zn ferrites are high saturation magnetization, dc electrical resistivity, Curie temperature, and moderate permeability. High saturation magnetization coupled with high dc electrical resistivity makes Ni–Zn nanoferrite system useful for variety of applications in particular as a magnetic core in transformers and inductors. However, the occupancy of magnetic ions among tetrahedral (A) and octahedral (B) sub-lattices plays a major role in tailoring the magnetic properties of the Ni–Zn ferrite. Room temperature magnetization data of $\text{Ni}_{0.5}\text{Zn}_{0.5}\text{Al}_x\text{Fe}_{2-x}\text{O}_4$ (where $x = 0.0, 0.25$) sintered at 1000 °C is shown in Fig. 7. As a normal behavior, the magnetization increases with increasing applied field and attains a maximum at higher fields. The observed decrease in magnetization is majorly

Fig. 6 SEM images of $\text{Ni}_{0.5}\text{Zn}_{0.5}\text{Al}_x\text{Fe}_{2-x}\text{O}_4$. **a** $x = 0.05$. **b** $x = 0.25$



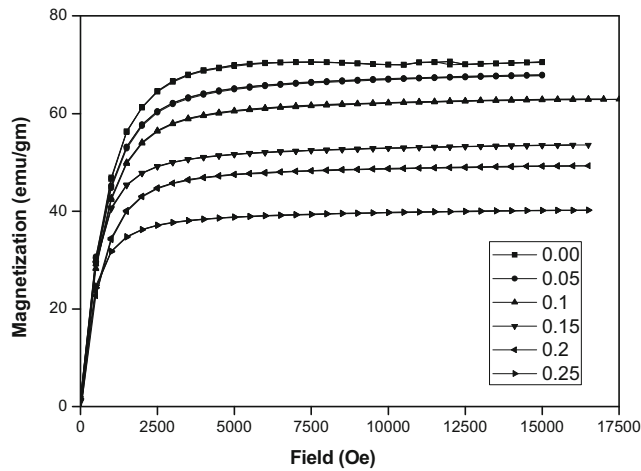


Fig. 7 Variation of magnetization (emu/g) with field (Oe) of $\text{Ni}_{0.5}\text{Zn}_{0.5}\text{Al}_x\text{Fe}_{2-x}\text{O}_4$

due to the substitution of non-magnetic Al^{3+} ions at the expense of magnetic ones (Fe^{3+} ions). The details regarding distribution of cations in the spinel lattice estimated from X-ray intensity calculations are reported elsewhere [14].

Coercivity is the minimum reverse magnetic field strength required to reduce the remenace to zero. All the ferrite samples exhibit low coercivity (Fig. 7) which resembles that all the samples belongs to the family of soft ferrites. Coercivity in a ferrite system is known to depend on various parameters like magneto crystalline anisotropy, lattice imperfections, dislocations, internal strains, particle size [28], and secondary phases [29]. The observed variations

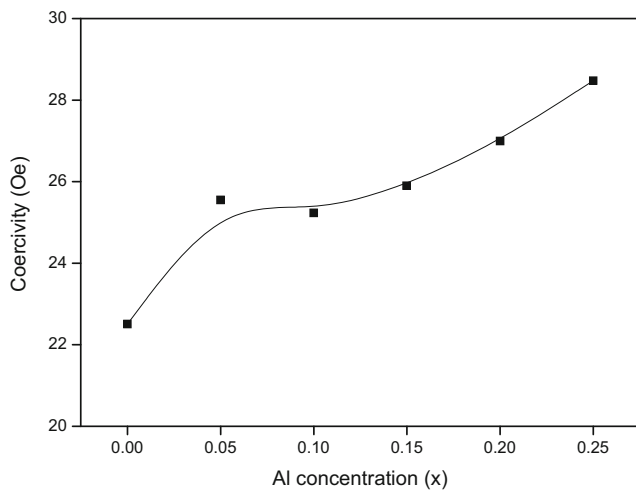


Fig. 8 Variation of coercivity with Al concentration of $\text{Ni}_{0.5}\text{Zn}_{0.5}\text{Al}_x\text{Fe}_{2-x}\text{O}_4$

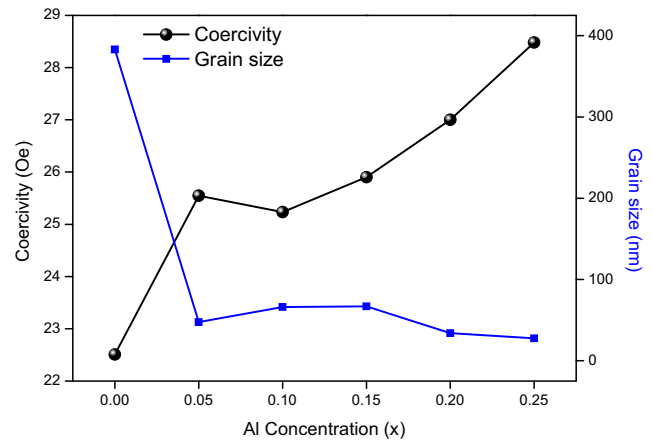


Fig. 9 Coercivity and grain size as a function of Al of $\text{Ni}_{0.5}\text{Zn}_{0.5}\text{Al}_x\text{Fe}_{2-x}\text{O}_4$ sintered at $1000\text{ }^\circ\text{C}$

in coercivity with Al concentration (x) for Ni-Zn-Al ferrite sintered at $1000\text{ }^\circ\text{C}$ are depicted in Fig. 8. Coercivity has been observed to increase with increasing Al concentration. It has been reported that the coercivity varies inversely with grain size, since samples with larger grain size have greater number of domain walls. Therefore, in the process of magnetization or demagnetization, the domain wall movement increases with the number of domain walls. The domain wall movement requires less energy than that required by domain rotation [30]. Hence, samples with larger grain size are expected to have low coercivity values. The dependence of coercivity on grain size as a function of Al concentration (x) is depicted in Fig. 9. In addition, the influence of porosity on coercivity is shown in Fig. 10. It is clear that (Fig. 10) coercive field and porosity follows the same trend. It is well established that, there has been two kinds of porosities, i.e., intragranular and intergranular, which could contribute the total porosity of the sample. If the intragranular porosity is predominant in the sample, this will increase the coercive field with increasing porosity. But in the present investigation, SEM images (Fig. 6) indicate that porosity comes mostly from the inter granular pores only, and thus, it is obvious that the field required for rotating the spins or bulge the domain walls is opposite to the amount of porosity present. The observed results are in accordance with the above arguments. Initial permeability and quality factor determine the performance of a soft ferrite. Generally, stoichiometry, grain structure, composition, concentration of impurity, saturation magnetization, magnetostriction, crystal anisotropy, and porosity significantly affect the initial permeability. The room temperature compositional dependence of initial permeability at 1 and 100 KHz for the Ni-Zn-Al ferrite sintered at $1000\text{ }^\circ\text{C}$ is shown in Fig. 11.

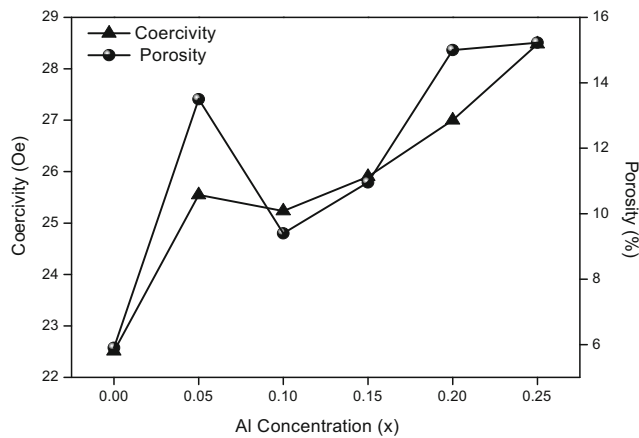


Fig. 10 Coercivity and porosity as a function of Al concentration of $Ni_{0.5}Zn_{0.5}Al_xFe_{2-x}O_4$ sintered at $1000\text{ }^\circ\text{C}$

The permeability of the ferrite was found to decrease with the increase in Al content. However, for the initial concentrations of Al, a rapid decrease has been observed up to $x = 0.05$, whereas insignificant variation has been observed above $x = 0.05$. This variation in initial permeability is explained as follows:

- (a) The decrease in permeability was primarily due to the substitution of Al ions for ferric ions into the ferrite lattice. In spinel ferrite, Zn^{2+} had a stronger preference for the tetrahedral site (“A” site), while Ni^{2+} ions (for which Zn is substituted) were located on octahedral site (“B” site). In the present investigation, substitution of Al^{3+} ions simultaneously reduces the concentration of Fe^{3+} ions from “A” and “B” sites. This in turn decreases the net magnetic moment of the lattice, since the neighboring magnetic spins “A” and “B” sites

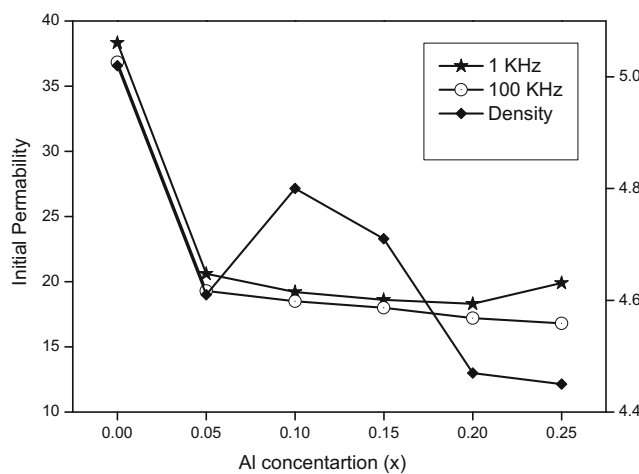


Fig. 11 Variation of initial permeability and density as a function of Al concentration

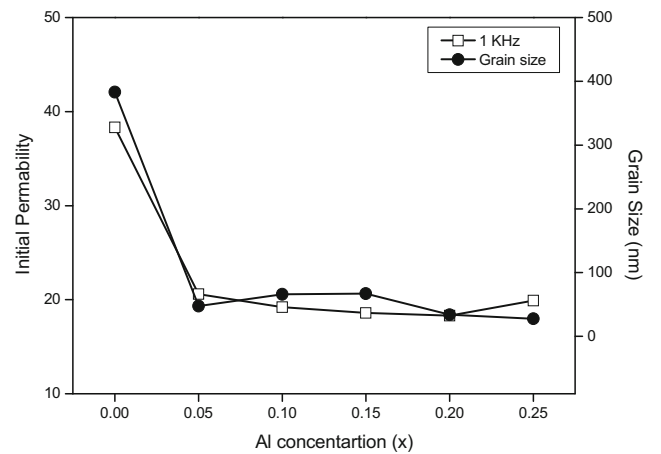


Fig. 12 Initial permeability and grain size of Ni–Zn–Al ferrite as a function of Al concentration

were coupled antiferromagnetically. In addition, saturation magnetization and permeability are interdependent properties; therefore, both the parameters follow the same trend with increasing Al concentration.

- (b) The second reason was attributed to the variation in bulk density with increased Al substitution results for initial gradual raise in initial permeability. For higher concentrations of Al, the decrease in density might reduce the permeability. Figure 11 clearly shows that permeability decreases with decreasing bulk density. An increase in the density (decrease in porosity) of ferrites not only resulted in the reduction of demagnetizing field due to decreased porosity but also raised the contribution due to rotation of spin, which in turn increased the permeability [31]. Porosity and other defects such as precipitates do not affect the initial permeability if they are confined to grain boundaries

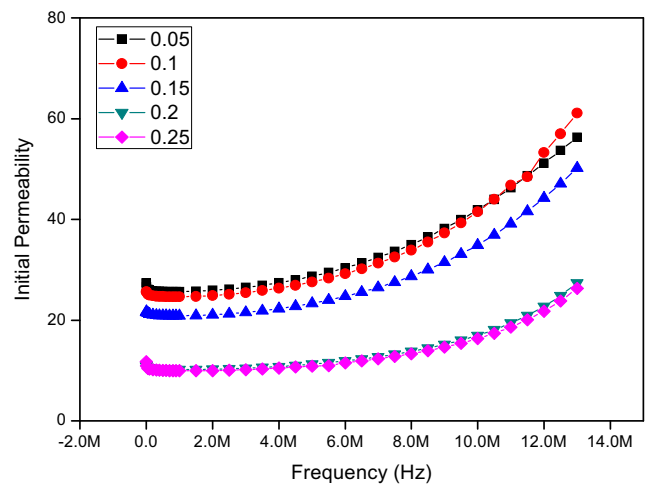


Fig. 13 Variation of permeability as a function of frequency of Ni–Zn–Al ferrite

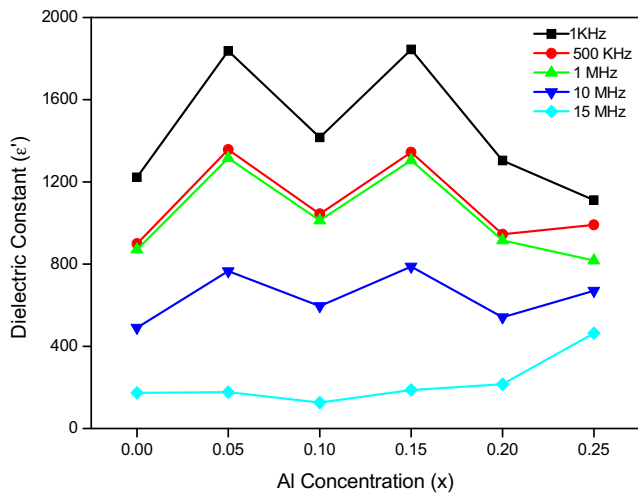


Fig. 14 Variation of dielectric constant as a function of Al concentration

(intergranular defects); otherwise, the initial permeability is severely decreased since defects act as pinning sites, reducing the volume swept by wall bowing.

- (c) Magnetic initial permeability is strongly dependent on the uniformity in the grain size and average grain diameter. According to Globus model [32], higher initial permeability is a result of higher bulk density and larger grain size. Since larger grains have more number of domain walls and the reversal of domain wall displacement contributes to initial permeability. The relation between initial permeability and grain size is as follows:

$$\mu_i = \frac{3\mu_0 M_s^2 D}{16\gamma_w}$$

where μ_i is the initial permeability, μ_0 is the permeability of free space, M_s is the saturation magnetization, D is the average grain size, and γ_w is the domain wall energy. Therefore, initial permeability is a linear function of grain size. Figure 12 indicates that permeability follows the same trend as grain size with increasing Al concentration.

- (d) Moreover, it was reported that initial permeability of ferrite is directly related to the saturation magnetization and inversely related to crystal magnetic anisotropy, and η is the magnetostriction constant [33]. Therefore, observed decreases in permeability imply the increase in anisotropy and magnetostriction constant.

The complex magnetic permeability of Ni–Zn–Al ferrite measured as a function of frequency and the dispersion spectra for the samples sintered at 1000 °C is shown in

Fig. 13. The relative permeability was stable for all the compositions (Fig. 13) up to 10 MHz and the cutoff frequencies of samples were above 13 MHz, since the maximum limit of the instrument is 13 MHz.

3.5 Dielectric Properties

Dielectric properties of the ferrites are sensitive to several factors such as the method of processing, sintering conditions, chemical composition, grain size, and size distribution. Also, the high electrical conductivity and the high dielectric constant of ferrites are go hand in hand, which indicates that materials with high dielectric constant possess low electric resistivity and vice versa [34]. The compositional dependence of dielectric constant (ϵ') at room temperature is shown in Fig. 14. It is found that dielectric constant decreases with increasing frequency and was not found at higher frequencies (15 MHz) and a distinct maxima is observed for Al compositions $x = 0.05, 0.15$. In the present investigation, the dielectric constant of undoped $\text{Ni}_{0.5}\text{Zn}_{0.5}\text{Fe}_2\text{O}_4$ is very low when compared to the same composition synthesized through standard ceramic route [35]. In spinel ferrites, the major contribution to dielectric constant is interfacial polarization. This kind of polarization arises due to the accumulation of charge carriers at the grain boundaries by the application of external electric field. Therefore, the higher the number of carriers reaching grain boundary results in greater polarization. The pertinent reason for the observed decrease in dielectric constant is due to the decrease in hopping between Fe^{3+} and Fe^{2+} ions at octahedral sites. The distribution of cations [14] proposed from X-ray intensity calculations suggests that substituted Al^{3+} ions replaces Fe^{3+} ions in both tetrahedral and octahedral sites simultaneously. Thus, the substitution of Al^{3+} ions reduces the concentration of Fe^{3+} ions at octahedral

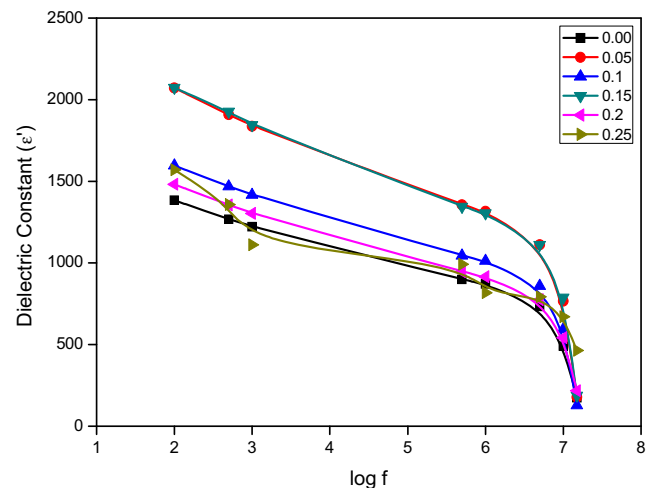


Fig. 15 Dielectric constant as a function of frequency of Ni–Zn–Al ferrite

sites. Consequently, this hinders the charge transfer between Fe^{2+} and Fe^{3+} ions and limits the accumulation at different grain boundaries, which in turn is expected to decrease the dielectric constant. However, a slender enhancement in the dielectric constant for the samples sintered at $1000\text{ }^\circ\text{C}$ is due to the occupancy of Al^{3+} ions on A sites causing some of the Fe^{3+} ions to migrate to B sites. This promotes charge transfer between ferrous and ferric ions which results in the observed increase in dielectric constant [36]. On the other hand, it was [37, 38] reported that inhomogeneities such as porosity and grain size are also one of the sources in reducing the dielectric constant, since pores will act as source of scattering centers. In addition to that, decrease in dielectric constant is in agreement with the observed improvement in the room temperature electrical resistivity [15] of Al-doped Ni–Zn ferrites resulting in a decrease in the interfacial polarization. Since dc-electrical resistivity increases with the substitution of Al due to the reduction of Fe^{3+} ions at the octahedral sites, which obstructs the flow of, charge carriers and lowers the build-up of interfacial polarization. Typical frequency variation curves of Ni–Zn–Al ferrite sintered at $1000\text{ }^\circ\text{C}$ is shown in Fig. 15. A higher value of dielectric constant at lower frequencies is observed for each sample, and the dielectric constant has been found to decrease rapidly with increasing frequency. The entire samples exhibit the similar trend which is a typical behavior of ferrites, and a similar trend was reported by several authors [39, 40]. The observed variation has been explained on the basis of Koops model. According to Koops, the ferrite ceramic is assumed to be composed of well conducting grains separated by highly resistive layers or grain boundaries [41]. These grain boundary layers are due to superficial reduction or oxidation of crystals in the porous material as a result of their direct contact with firing temperature. In case of nanoferrite, the decrease in grain size increases the number of grain boundaries. Thus, the applied voltage drops across the grain boundaries causes interfacial polarization due to the free charges on the grain boundaries. Koops proposed that grain boundaries contribute to dielectric constant at lower frequencies and the conducting grains are effective at higher frequencies which results in a low dielectric constant. Another possible explanation for the decrease of dielectric constant with increasing frequency is given as follows.

As mentioned earlier, the interfacial polarization contributes in principal to the observed dielectric constant at low frequencies. This results from the accumulation of charges at the grain boundaries through hopping. In Ni–Zn ferrite, conduction occurs between Fe^{3+} and Fe^{2+} ions, Ni^{2+} and Ni^{3+} ions at octahedral sites through hoping mechanism. Therefore, the greater the hopping, the more number of charge carriers will reach the grain boundary through

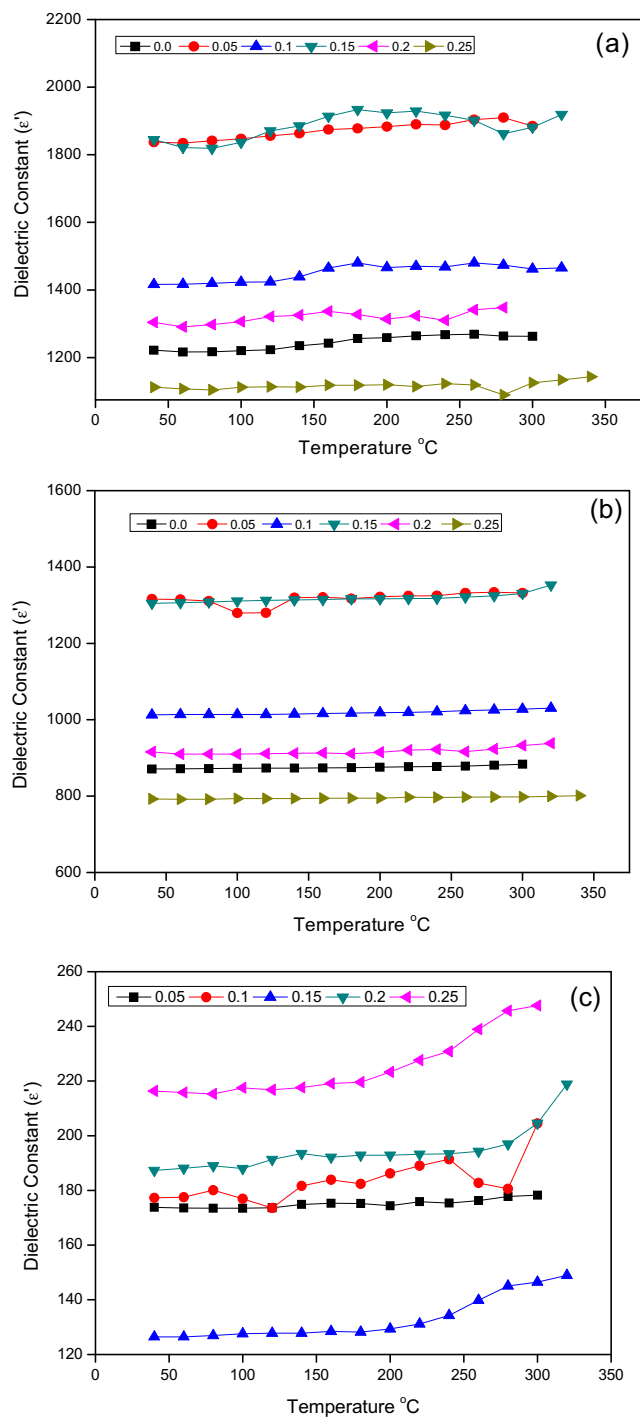


Fig. 16 Dielectric constant as a function of temperature of Ni–Zn–Al ferrite at different frequencies. **a** $x = 1\text{ KHz}$. **b** $x = 1\text{ MHz}$. **c** $x = 15\text{ MHz}$

this mechanism. If the concentration of Fe^{2+} ions and resistance of the grain boundary is high enough, electrons pile up at the boundary on application of alternating field and this in turn produces polarization. However, with increasing the frequency, the electron reverses their direction of

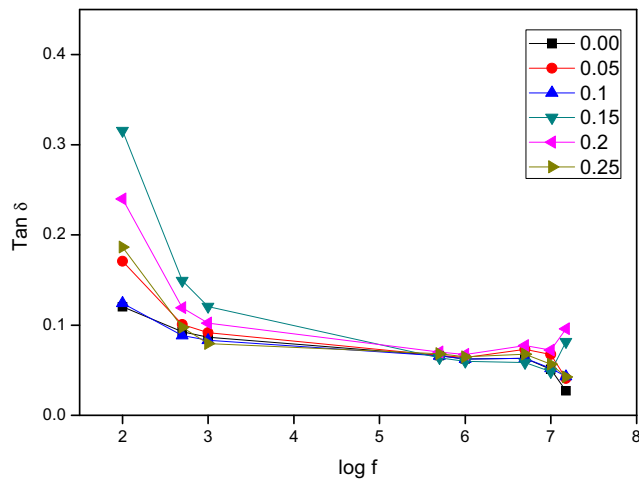


Fig. 17 Dielectric loss tangent as a function of frequency Ni-Zn-Al ferrite sintered at 1000 °C

motion more often. Due to this, the probability of the electrons reaching the grain boundary decreases [42]. Hence, the dielectric constant value decreases with increasing frequency. Figure 16 depicts the temperature dependence of dielectric constant for Ni–Zn–Al ferrite sintered at 1000 °C. It is clear that dielectric constant value is very large at lower frequencies (1 KHz) and decreases with increasing temperature. The interfacial and dipolar polarization plays a major role at low frequencies around 1 KHz and are temperature dependent. At higher frequencies, the dielectric constant is usually intrinsic with contributions arising only from the normal ionic and the electronic polarizations. The interfacial polarization increases with increasing temperature which is due to the creation of crystal defects [43] and dipolar polarization decreases with increasing temperature. In the present investigation, significant raise in the dielectric constant with increasing temperature for the sample $x = 0.0$ (Fig. 16) is due to the dominance of interfacial polarization. Also, this kind of polarization is due to the pile up of charge carriers at the grain boundaries. Therefore, with increasing temperature, the density of charges reaching the boundary is also increased. This causes a rapid increase in the polarization. However, after the substitution of Al, an insignificant variation in the dielectric constant is observed for the all the substituted samples.

The loss tangent infers the energy loss in the sample. The variation of dielectric loss tangent ($\text{Tan } \delta$) as a function is shown in Fig. 17. It is clear that dielectric loss tangent decreases with increasing frequency for all the samples similar to dielectric constant (Fig. 15). The observed behavior is due to Maxwell-Wagner type interfacial polarization [44, 45]. It is reported that stoichiometry, number of Fe^{2+} ions, and structural homogeneity influences

the values of dielectric loss tangent [46]. It is clear that dielectric loss is higher at lower frequencies and lower at higher frequencies. According to Koops phenomena, ferrite samples consists of two layers, i.e., grains and grain boundaries, where the resistivity of grain boundaries is larger than the resistivity of grains, which leads to the accumulation of charges at the interfaces between grains and grain boundaries and contributes to the polarization and consequently to dielectric loss at low frequencies, whereas at higher frequencies, most of the charges cannot follow the frequency of the applied field and their contribution to the polarization ceases. Therefore, dielectric loss decreases with rise in frequency and reaches almost constant value.

4 Conclusions

In the present study, the changes in the structural and magnetic properties of Al substituted $\text{Ni}_{0.5}\text{Zn}_{0.5}\text{Fe}_2\text{O}_4$ ferrite synthesized by CGAC method has been studied. The following conclusions have been drawn from the above discussed results.

- (i) XRD confirms the single-phase spinel formation. The crystallite size of Al substituted Ni–Zn ferrite is around 62–57 nm. This shows that the present method of preparation citrate-gel autocombustion method produces the ferrite in nanophase. The other structural parameters such as shared and unshared bond lengths and bond angles have been calculated to understand the effect of Al on the structural properties of Ni–Zn ferrite. The decrease in interionic distances and bond lengths affects the interaction between magnetic ions at A and B sites. The prominent absorption bands in infrared spectra support the spinel phase of the synthesized Ni–Zn–Al ferrite.
- (ii) Morphological studies show that method of preparation and Al dopant affects the microstructure. Grain morphology, uniformity, and homogeneity of the ferrite changes with the addition of Al. Grains are found to be spherical in shape with well-defined boundaries and uniformly distributed for all the samples. The grain size decreased with increasing Al concentration.
- (iii) Saturation magnetization and permeability follows the same decreasing trend with increasing Al concentration. These variations are due to the weakening of exchange interactions and grain size due to the substitution of nonmagnetic Al. The coercivity is very low for all the samples, which makes them useful for microwave devices, security, switching, and sensing applications. The observed decrease in initial perme-

ability with increasing Al concentration is due to the decrease in grain size, Fe^{3+} ion concentration, and variation in bulk density.

- (iv) Dielectric constant and dielectric loss decrease with increasing Al concentration and with applied frequency.

References

- Kondo, K., Chiba, T., Yamada, S.: *J. Magn. Magn. Mater.* **541**, 254 (2003)
- Mohd. Hashim, A., Kumar, S., Koo, B.H., Shirsath, S.E., Mohammed, E.M., Shah, J., Kotnala, R.K., Choi, H.K., Chung, H., Kuma, R.: *J. Alloys Comp.* **518**, 11 (2012)
- Venkatesh, D., Himavathi, G., Ramesh, K.V.: *J. Super. Nov. Magn.* **28**, 2801 (2015)
- Mohamed, M.B., El Sayed, K.: *Compos. Part B* **56**, 270 (2014)
- Bahiraeei, H., Zargar Shoushtari, M., Gheisari, K., Ong, C.K.: *J. Magn. Magn. Mater.* **371**, 29 (2014)
- Bueno, A.R., Gregori, M.L., Nobrega, M.C.S.: *Mat. Chem. Phys.* **105**, 229 (2007)
- Varaprasad, B.B.V.S.: *Mod. Phys. Lett. B* **28**, 1450155 (2014)
- Goldman, A.: *Modern ferrite technology*, p. 87. Van Nostrand Reinhold, New York (1990)
- Li, M., Zhou, Z., Liu, M., Lou, J., Oates, D.E., Dionne Ming, G.F., Wang, L., Sun, N.X.: *J. Phys. D. Appl. Phys.* **46**, 275001 (2013)
- Eltabey, M.M., El-Shokrofy, K.M., Gharbia, S.A.: *J. Alloy Comp.* **509**, 2473 (2011)
- Vishnu Prasad Rao, K., Purushotham, Y., Chandel, J.S.: *Cryst. Res. Technol.* **31**, 329 (1996)
- Lakhani, V.K., Modi, K.B.: *J. Phys. D. Appl. Phys.* **44**, 245403 (2011)
- Rajesh Babu, B., Prasad, M.S.R., Ramesh, K.V., Purushotham, Y.: *Mat. Chem. Phys.* **148**, 585 (2014)
- Rajesh Babu, B., Prasad, M.S.R., Ramesh, K.V.: *Int. J. Modern Phys. B* **29**, 1550032 (2015)
- Rajesh Babu, B., Ramesh, K.V., Prasad, M.S.R., Purushotham, Y.: *Mod. Phys. Lett. B* **29**, 1550151 (2015)
- Valenzuela, R.: *Magnetic Ceramics*. Cambridge Press (1994)
- Vegard, L.: *Z. Phys.* **5**, 17 (1921)
- Sickafus, K.E., Wills, J.M., Grimes, N.W.: *J. Am. Ceram. Soc.* **82**, 3279 (1999)
- Lakhani, V.K., Pathak, T.K., Vasoya, N.H., Modi, K.B.: *Sol. Sta. Sci.* **13**, 539 (2011)
- Goodenough, J.B.: *J. Phys. Chem. Sol.* **6**, 287 (1958)
- Kanamori, J., Phys, J.: *Chem. Sol.* **10**, 87 (1959)
- Williamson, G.K., Hall, W.H.: *Acta. Metal.* **1**, 22 (1953)
- Tang, G.D., Shang, Z.F., Zhang, X.Y., Xu, J., Li, Z.Z., Zhen, C.M., Qi, W.H., Lang, L.L.: *Phys. B* **463**, 26 (2015)
- Lakhani, V.K., Pathak, T.K., Vasoya, N.H., Modi, K.B.: *Sol. Sta. Sci.* **13**, 539 (2011)
- Baykal, A., Genç, F., Elmal, A.Z., Gökçe, S., Sertkol, M., Sozeri, H.: *J. Inorg. Organomet. Polym.* (2015). doi:10.1007/s10904-015-0288-0
- Maghsoudi, I., Hadianfard, M.J., Shokrollahi, H.: *J. Alloys Compd.* **481**, 539 (2009)
- Hoque, S.M., Choudhry, Md.A., Islam, Md.F.: *J. Magn. Magn. Mater.* **251**, 292 (2002)
- Manjura Hoque, S., Samir Ullah, M., Khan, F.A., Hakim, M.A., Saha, D.K.: *Phys. B Condens. Matter* **406**, 1799 (2011)
- Verma, V., Gairola, S.P., Pandey, V., Kotanala, R.K., Su, H.: *Sol. Sta. Comm.* **148**, 117 (2008)
- De Fazio, E., Bercoff, P.G., Jacobo, S.E.: *J. Magn. Magn. Mater.* **323**, 2813 (2011)
- Shrotri, J.J., Kulkarni, S.D., Deshpande, C.E., Mitra, A., Sainkar, S.R., Anil Kumar, P.S., Date, S.K.: *Mat. Chem. Phys.* **59**, 1 (1999)
- Valenzuela, R.: *Magnetic Ceramics*. National University of Mexico (1994)
- Yue, Z., Li, L., Zhou, J., Zhang, H., Gui, Z.: *J. Magn. Magn. Mater.* **233**, 224 (2001)
- Koops, C.G.: *Phys. Rev.* **83**, 121 (1951)
- Yin, W.S., Hassan, J., Hashim, M.: *AIP Conf. Proc.* **1250**, 325 (2010)
- Mangalaraja, R.V., Ananthakumar, S., Manohar, P., Gnanam, F.D.: *J. Magn. Magn. Mater.* **253**, 56 (2002)
- Verma, S., Chand, J., Singh, M.: *Adv. Mat. Lett.* **4**, 310 (2013)
- Batoo, K.M., Kumar, S., Lee, C.G., Alimuddin, K.: *Curr. Appl. Phys.* **9**, 826 (2009)
- Verma, A., Chatterjee, R.: *J. Magn. Magn. Mater.* **306**, 313 (2006)
- Narayanaswamy, A., Sivakumar, N.: *Bull. Mater. Sci.* **31**, 373 (2008)
- Sheik, A.D., Amthe, V.L.: *J. Mater. Sci.* **43**, 2018 (2008)
- Ajmal, M., Maqsood, A.: *Mater. Lett.* **62**, 2077 (2008)
- Kony, E.: *Egypt. J. Sol.* **27**, 285 (2004)
- Maxwell, C.: *A Treatise on Electricity and Magnetism*. Oxford University Press, Oxford (1988)
- Wagner, K.W.: *Amer. J. Phys.* **40**, 817 (1973)
- Nasir, S., Anis-ur-Rehman, M.: *Phys. Scr.* **84**, 025603 (2011)